Production cross sections of $^{243-248}$No isotopes in fusion reactions

Yu-Hai Zhang,[1,2] Gen Zhang,[3] Jing-Jing Li,[2] Zhong Liu,[4] A. V. Yeremin,[5,6] and Feng-Shou Zhang[1,2,7,*]

[1]*The Key Laboratory of Beam Technology and Energy Material, College of Nuclear Science and Technology, Beijing Normal University, Beijing 100875, China*

[2]*Institute of Radiation Technology, Beijing Academy of Science and Technology, Beijing 100875, China*

[3]*School of Physical Science and Technology, Guangxi University, Nanning 530004, China*

[4]*Institute of Modern Physics, Chinese Academy of Sciences, Lanzhou 730000, China*

[5]*Flerov Laboratory of Nuclear Reactions, JINR, Dubna 141980, Russia*

[6]*Dubna State University, Dubna 141980, Russia*

[7]*Center of Theoretical Nuclear Physics, National Laboratory of Heavy Ion Accelerator of Lanzhou, Lanzhou 730000, China*

(Received 5 May 2022; accepted 20 July 2022; published 29 July 2022)

The production of $^{243-254}$No is investigated within the framework of the improved quantum molecular dynamical model incorporated with a statistical model. The calculated results of the ^{48}Ca + ^{208}Pb fusion reaction can reproduce the experimental data well. The impact parameter and the incident energy influence the fusion probability and the lifetime of the neck in fusion reaction process. Furthermore, the evaporation residue cross sections of ^{40,44,48}Ca + ^{208}Pb, ^{20}Ne + ^{233,235,238}U, ^{16}O + ^{242}Pu, and ^{26}Mg + ^{232}Th reactions are calculated. From investigation, the more neutrons there are in the projectile or target for the same projectile-target combination, the larger evaporation residue cross sections will be. Six unknown isotopes $^{243-248}$No are predicted with maximum evaporation residue cross sections 0.061 pb, 2.250 pb, 0.005 nb, 0.530 nb, 0.432 nb, and 3.518 nb, respectively. The corresponding fusion reactions are ^{208}Pb(^{40}Ca, $5n$)^{243}No, ^{208}Pb(^{40}Ca, $4n$)^{244}No, ^{208}Pb(^{40}Ca, $3n$)^{245}No, ^{208}Pb(^{40}Ca, $2n$)^{246}No, ^{233}U(^{20}Ne, $6n$)^{247}No, and ^{233}U(^{20}Ne, $5n$)^{248}No, respectively.

DOI: 10.1103/PhysRevC.106.014625

I. INTRODUCTION

Since the discovery of superheavy nuclei [1], great progress in the synthesis of new heavy and superheavy nuclei by fusion reactions has been achieved in recent years. ^{262}Bh, ^{265}Hs, ^{267}Mt, ^{269}Ds, and ^{272}Rg have been synthesized by using ^{208}Pb or ^{209}Bi targets [2–6]. Twenty-nine new heavy nuclides with $Z = 112$–118 have been produced successfully in the fusion reactions of actinide targets with ^{48}Ca or ^{70}Zn beams [7–17]. Currently, although the No isotopes produced in experiments are rather neutron deficient, the predicted position of the proton drip line still has not been reached. Therefore, the production of unknown No isotopes, especially in fusion reactions, has attracted extensive attention both experimentally and theoretically.

The element nobelium ($Z = 102$) was first discovered by Donets *et al.* and Zager *et al.* with the reactions ^{243}Am(^{15}N, $4n$)^{254}No and ^{238}U(^{22}Ne, $6n$)^{254}No in 1965 [18,19]. Up to now, only 13 nobelium isotopes ($^{249-260,262}$No) have been produced [18–30]. The synthesis methods of nobelium isotopes are summarized in Table I. The abbreviations FE, MNT, and EC in the Table I represent fusion-evaporation reaction, multinucleon transfer reaction, and electron capture, respectively. $^{249-259}$No were produced by using the FE reaction, ^{260}No was the only isotope obtained by using the MNT reaction, and ^{262}No was observed in the β^+ decay of ^{262}Lr and identified through its spontaneous fission. The production cross sections of the isotopes $^{252-254}$No were measured for the FE reactions of ^{22}Ne + ^{236,238}U and ^{26}Mg + ^{232}Th by using the kinematic separator VASSILISSA [31,32]. The first evidence of at least one high-K isomer in ^{256}No was obtained by using the highly asymmetric FE reaction ^{238}U(^{22}Ne, $4n$)^{256}No [33]. Recently, with the reaction of complete fusion of ^{48}Ca ions with ^{204}Pb, ^{249}No has been identified in an experiment carried out with the SHELS separator [20]. ^{249}No was also observed in the α decay of the new isotope ^{253}Rf [21]. Some semiclassical and microscopic models are developed to describe the fusion processes in low-energy heavy-ion collisions. The semiclassical models such as the two-step model [34], the dinuclear system (DNS) model [35–39], the fusion-by-diffusion model [40–42]. and some others [43–46] have successfully described the production cross sections of heavy and superheavy nuclei. For instance, the production of No isotopes $^{249-263}$No were studied in FE reactions based on the DNS model [47]. The new neutron-rich isotopes $^{261-263}$No were calculated using ^{242}Pu(^{22}O, $3n$)^{261}No, ^{244}Pu(^{22}O, $4n$)^{262}No, and ^{244}Pu(^{22}O, $3n$)^{263}No reactions, and the corresponding maximum evaporation residue cross sections are 0.628, 4.649, and 1.638 μb, respectively. The microscopic dynamics models, such as the time-dependent Hartree-Fock (TDHF) model [48–51] and improved quantum molecular dynamics (ImQMD) model [52–54] have also shown rea-

*Corresponding author: fszhang@bnu.edu.cn

TABLE I. A brief summary of the No isotopes.

Isotope	E_{lab} (MeV)	Method	Channel	Reaction	References
^{249}No	225.4	FE	$3n$	^{48}Ca + ^{204}Pb	[20]
		α decay		^{253}Rf	[21]
^{250}No	213.5–242.5	FE	$4n$	^{48}Ca + ^{206}Pb	[22]
	213.5–242.5	FE	$2n$	^{48}Ca + ^{204}Pb	[22]
^{251}No	78–90	FE	$5n$	^{12}C + ^{244}Cm	[23]
^{252}No	96	FE	$5n$	^{18}O + ^{239}Pu	[24]
^{253}No	102	FE	$5n$	^{16}O + ^{242}Pu	[24]
^{254}No		FE	$6n$	^{22}Ne + ^{238}U	[18]
	82–84	FE	$4n$	^{15}N + ^{243}Am	[18,19]
^{255}No	177	FE	$5n$	^{22}Ne + ^{238}U	[25]
^{256}No	110–120	FE	$4n$	^{22}Ne + ^{238}U	[26]
^{257}No	63–68	FE	$4n$	^{13}C + ^{248}Cm	[23]
^{258}No	67.6	FE	$3n$	^{13}C + ^{248}Cm	[27]
^{259}No	88–106	FE	$3n$	^{18}O + ^{248}Cm	[28]
^{260}No	99	MNT		^{18}O + ^{254}Es	[29]
^{262}No		EC		^{262}Lr	[30]

sonable success in describing the mechanisms of heavy-ion reactions.

The aim of this work is to produce unknown neutron-deficient nobelium isotopes by using the ImQMD model via ^{40,44,48}Ca + ^{208}Pb, ^{20}Ne + ^{233,235,238}U, ^{16}O + ^{242}Pu, and ^{26}Mg + ^{232}Th reactions. The deexcitation processes are treated with the statistical model.

This paper is organized as follows. In Sec. II, we describe the ImQMD model. The results and discussion are presented in Sec. III. Finally, we summarize the main conclusions in Sec. IV.

II. THE MODEL

The ImQMD model is an improved version of the quantum molecular dynamics (QMD) model [54,55]. The standard Skyrme interaction with the omission of the spin-orbit interaction is adopted to describe the bulk and surface properties of nuclei [56]. The stochastic two-body collision process is added to the time evolution by the Hamilton equation of motion. In order to improve the stability of an individual nucleus, the Fermi constraint proposed by Papa *et al.* is taken into account in this model [57]. Considering the collision part, an isospin dependent nucleon-nucleon scattering cross section and Pauli blocking are used in this model.

A. Brief introduction of the ImQMD model

As in the original QMD model, each nucleon is represented by a Gaussian wave packet of coherent states in the ImQMD model:

$$\phi_i(\mathbf{r}) = \frac{1}{(2\pi\sigma_r^2)^{3/4}} \exp\left[-\frac{(\mathbf{r}-\mathbf{r}_i)^2}{4\sigma_r^2} + \frac{i}{\hbar}\mathbf{r}\cdot\mathbf{p}_i\right], \tag{1}$$

where $\mathbf{r}_i$ and $\mathbf{p}_i$ are the wave packet centers of the ith particle in the coordinate and momentum space, respectively. σ_r represents the spatial spread of the wave packet. By applying the Winger transform to the wave function, the one-body phase space distribution function under quantum mechanical conditions can be obtained. Hence, the density distribution function ρ and momentum distribution function g of a system read:

$$\rho(\mathbf{r}) = \sum_i \frac{1}{(2\pi\sigma_r^2)^{3/2}} \exp\left[-\frac{(\mathbf{r}-\mathbf{r}_i)^2}{2\sigma_r^2}\right], \tag{2}$$

$$g(\mathbf{p}) = \sum_i \frac{1}{(2\pi\sigma_p^2)^{3/2}} \exp\left[-\frac{(\mathbf{p}-\mathbf{p}_i)^2}{2\sigma_p^2}\right]. \tag{3}$$

The propagation of nucleons is governed by Hamiltonian equations of motion under the self-consistently generated mean field:

$$\dot{\mathbf{r}}_i = \frac{\partial H}{\partial \mathbf{p}_i}, \qquad \dot{\mathbf{p}}_i = -\frac{\partial H}{\partial \mathbf{r}_i}. \tag{4}$$

The initial conditions of the reaction, such as the properties of projectile and target nuclei, are of vital importance for studying low-energy heavy-ion reactions using the microscopic transport model [58]. In Fig. 1, we check the time evolution of binding energies and root-mean-square charge radii for ^{48}Ca and ^{208}Pb calculated by the ImQMD model with parameter set IQ3a. One can see that their binding energies and root-mean-square charge radii remain constant with a very small fluctuation and the bound nuclei evolve stably without spurious emission for a period of time of about 3000 fm/c, which is essential for applications to fusion reactions of heavy nuclei.

The Hamiltonian H consists of the kinetic energy $T = \sum_i \frac{p_i^2}{2m}$, the nuclear interaction potential energy, and the Coulomb interaction potential energy,

$$H = T + U_{\rm loc} + U_{\rm Coul}, \tag{5}$$

where $U_{\rm loc} = \int V_{\rm loc}(\mathbf{r})d\mathbf{r}$ is obtained from the standard Skyrme energy density functional,

$$V_{\rm loc} = \frac{\alpha}{2}\frac{\rho^2}{\rho_0} + \frac{\beta}{\gamma+1}\frac{\rho^{\gamma+1}}{\rho_0^{\gamma}} + \frac{g_{\rm sur}}{2\rho_0}(\nabla\rho)^2 + g_\tau\frac{\rho^{\eta+1}}{\rho_0^{\eta}} + \frac{C_s}{2\rho_0}[\rho^2 - k_s(\nabla\rho)^2]\delta^2, \tag{6}$$

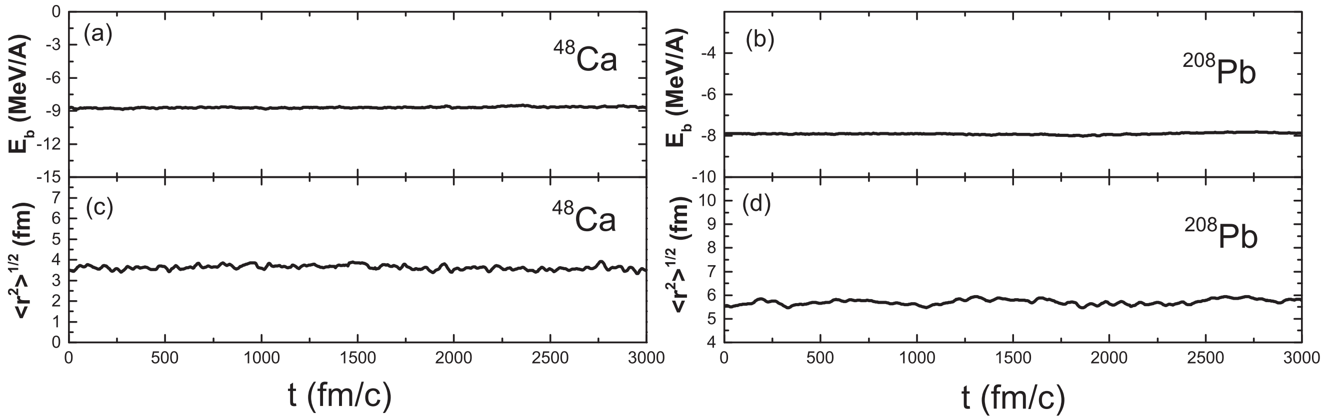

FIG. 1. The time evolution of binding energies and root-mean-square charge radii for ^{48}Ca and ^{208}Pb calculated by the ImQMD model with parameter set IQ3a.

where $\delta = (\rho_n - \rho_p)/(\rho_n + \rho_p)$ is the isospin asymmetry. U_{Coul} is the Coulomb interaction potential energy which includes the contribution of the direct and exchange terms.

In the ImQMD code, nucleon-nucleon collisions are determined as follows: first, only nucleon pairs with relative distance $r_{ij} < 3.5$ fm and energy $s = (p_i + p_i)^2 > 3.556$ GeV^2, where $p_i = (E_i, \vec{p}_i)$, are considered in order to speed up simulations; then, the attempted collisions are determined by using the transverse and longitudinal distances of the colliding pairs. More detailed descriptions of the nucleon-nucleon collisions term can be found in Ref. [54].

To describe the fermionic nature of the N-body system and to improve the stability of an individual nucleus, the modified Fermi constraint, which was previously proposed by Papa *et al.* [57], is adopted. The phase space occupation probability $\bar{f}_i$ of the ith particle is checked during the propagation of nucleons. If $\bar{f}_i > 1$, a violation of the Pauli principle, the momentum of the particle is randomly changed by a series of two-body elastic scatterings between this particle and its neighboring particles, together with Pauli blocking condition being checked after the momentum redistribution.

In this work, we set the z axis as the beam direction and the x axis as the impact parameter direction. The initial distance of the center of mass between the projectile and target is 30 fm. The dynamic simulation is stopped at 2000 fm$/c$ and 500 events for each impact parameter simulated in this work. The range of the impact parameters in the calculations is from 0 to b_{max} fm. $b_{max} = R_p + R_T$, where R_p and R_T denote the radii of the projectile and target, respectively.

Besides, we use the parameter set of IQ3a (see Table II) and set the wave-packet width $\sigma_r = 1.3$ fm in our calculations. The binding energy of symmetric nuclear matter at saturation density ρ_0 is -15.92 MeV. The corresponding value of the incompressibility coefficient of nuclear matter is 225 MeV. The slope parameter of the symmetry energy parameter is 77 MeV. Additionally, the parameter set IQ3a has been tested for describing the fusion process in Ref. [59].

B. The calculation on evaporation residue cross sections

In the ImQMD model, we judge whether a fusion event is formed according to the following conditions: If two independent nuclei can overcome the Coulomb barrier and fuse together (the distance between the two nuclei <3 fm), and the density of fused monomer can be maintained all the time in the process of the compound nucleus rotating one to several times or oscillating several times along the diameter, then such an event is considered fusion event.

We first create certain reaction events at each incident energy $E_{\text{c.m.}}$ and impact parameter b, then count the number of fusion events, and finally we obtain the cross sections by using this formula:

$$\begin{aligned}\sigma_{\text{fus}}(E_{\text{c.m.}}, b) &= 2\pi \int_0^{b_{max}} b g_{\text{fus}}(E_{\text{c.m.}}, b) db \\ &= 2\pi \sum b g_{\text{fus}}(E_{\text{c.m.}}, b) \triangle b,\end{aligned} \tag{7}$$

where $g_{\text{fus}}(E_{\text{c.m.}}, b)$ is the probability of fusion reactions. For the production of superheavy nuclei, we need to consider the effects of fission and neutron evaporation on the cross sections. For each impact parameter b, angular momentum J of compound nucleus is calculated by the coordinates and momentums of all nucleons in the rest frame. Hence, the evaporation residue cross section in heavy-ion fusion reactions is calculated as follows:

$$\sigma_{ER}(E_{\text{c.m.}}, J) = \sigma_{\text{fus}}(E_{\text{c.m.}}, J) \times W_{\text{sur}}(E_{\text{c.m.}}, J), \tag{8}$$

TABLE II. Model parameters (IQ3a) adopted in this work.

α (MeV)	β (MeV)	γ	g_{sur} (MeV fm^2)	g_τ (MeV)	η	C_S (MeV)	k_s (fm^2)	ρ_0 (fm^{-3})
−207	138	7/6	16.5	14.0	5/3	34.0	0.40	0.165

where $W_{\rm sur}(E_{\rm c.m.}, J)$ is the survival probability. In the ImQMD model, the excitation energy of an excited compound nucleus is calculated as $E^*_{CN} = E_{tot} - E_b$. Here, E_{tot} and E_b denote the total and binding energies in the ground state, respectively. The total energy of a compound nucleus is the sum of all kinetic and potential energy of all nucleons in the body frame. Based on a statistical model [60–62], the survival probability under the evaporation of x ($x > 1$) neutrons is written as [63]

$$W_{\rm sur}(E^*_{\rm CN}, x, J) = P(E^*_{\rm CN}, x, J) \times \prod_{i=1}^{x}\left[\frac{\Gamma_n(E^*_i, J)}{\Gamma_n(E^*_i, J) + \Gamma_f(E^*_i, J)}\right]_i, \quad (9)$$

where $P(E^*_{\rm CN}, x, J)$ is the realization probability of the xn-evaporation channel with excitation energy $E^*_{\rm CN}$ and angular momentum J. Γ_n and Γ_f are the widths of the neutron emission and fission, which are given by Weisskopf's evaporation theory and the formula of Bohr and Wheeler. E^*_i is the excitation energy before the evaporation of the i th neutron, which satisfies the relation $E^*_{i+1} = E^*_i - B^n_i - 2T_i$. We calculated the fission barrier of the nucleus before evaporating the i th nucleus using this formula:

$$B^f_i = B^{LD}_f + B^M_f(E_i = 0)\exp(-E^*_i/E_d), \quad (10)$$

where $E_d = 5.48A^{1/3}/(1 + 1.3A^{-1/3})$ is the shell damping factor. B^{LD}_f is macroscopic fission barrier, which is calculated using a droplet model. B^M_f is microscopic fission barrier, which is taken from [64]. For the superheavy nucleus $Z > 106$, the fission barrier is mainly determined by the shell correction energy, and the shell damping factor is set as a constant $E_d = 20$ MeV. The realization probability of evaporating x neutrons ($x > 1$) is written as

$$P(E^*_{\rm CN}, x, J) = I(\Delta_x, 2x - 3) - I(\Delta_{x+1}, 2x - 1), \quad (11)$$

where the functions I and Δ have the following forms:

$$I(z, m) = \frac{1}{m!}\int_0^z u^m e^{-u} du, \quad (12)$$

$$\Delta_x = \frac{1}{T}\left(E^*_{\rm CN} - \sum_{i=1}^{x} B^n_i\right). \quad (13)$$

The probability of evaporating one neutron is given by the following formula [65,66]:

$$P(E^*_{\rm CN}, 1, J) = \exp\left(-\frac{(E^*_{\rm CN} - B_n - 2T)^2}{2\sigma^2}\right), \quad (14)$$

where $\sigma = 2.2$ MeV. For the details of the calculation of E^*_i and $P(E^*_{\rm CN}, x, J)$, see Refs. [65,67,68].

C. The test of the ImQMD model

Attempt to produce new neutron-deficient isotopes of No, the fusion reaction systems ^{44,48}Ca + ^{204,206,208}Pb were studied in the experiment [69–71]. It is clearly shown that neutron excess at incident projectiles leads to higher evaporation residue cross sections [71]. Hence, in order to test the feasibility of using the ImQMD model, we calculated the capture cross sections and the excitation functions of the xn-evaporation channels ($x = 2$–5) of the ^{48}Ca + ^{208}Pb fusion reaction. Figure 2(a) shows the comparisons between calculated capture cross sections and the experimental data in the reaction ^{48}Ca + ^{208}Pb. One can see that the calculated results of two models (ImQMD and DNS) are in good agreement with the experimental data [69].

Figure 2(b) shows the excitation functions in the xn-evaporation channels ($x = 2$–5) for the ^{48}Ca + ^{208}Pb reaction. One can see that the experimental data can be reproduced well. At incident energy above the Coulomb barrier, more neutrons will be emitted in the deexcitation process. Meanwhile, the fission channel becomes more and more important at high incident energy states. As a result, the calculated peak values of the $3n$, $4n$, and $5n$ channels are rapidly decreasing compared to that of the $2n$ channel.

The evaporation residue cross sections of known $^{249–254}$No isotopes in different FE reactions are given in Table III. One finds that the experimental data are well reproduced by the ImQMD model in the reactions of ^{44,48}Ca + ^{208}Pb. The fusions of ^{40,44,48}Ca nuclei with ^{208}Pb at near-barrier incident energies generate low-excited compound nuclei. The fusions of these reactions are called cold fusion. The fusions of ^{20}Ne, ^{16}O, and ^{26}Mg nuclei with ^{233,235,238}U, ^{242}Pu, and ^{232}Th targets lead to the formation of quite-high-excitation-energy compound nuclei; these reactions are called hot fusion.

From Table III, it is obvious that the known $^{249–253}$No isotopes can be synthesized in the hot-fusion reactions ^{233}U(^{20}Ne, $4n$)^{249}No, ^{235}U(^{20}Ne, $5n$)^{250}No, ^{235}U(^{20}Ne, $4n$)^{251}No, ^{242}Pu(^{16}O, $6n$)^{252}No, and ^{242}Pu(^{16}O, $5n$)^{253}No, respectively, with rather large cross sections. The corresponding maximum evaporation residue cross sections are 4.702 nb, 16.543 nb, 19.419 nb, 168.080 nb, and 465.750 nb, respectively. ^{254}No was synthesized in the cold-fusion reaction ^{208}Pb(^{48}Ca, $2n$)^{254}No, and the maximum evaporation residue cross section is 4289.070 nb.

It can also be found that there are some differences between two models from Table III. When calculating a cold-fusion reaction (^{44,48}Ca + ^{208}Pb), the ER cross sections calculated by the DNS model are higher than those of the ImQMD model. When calculating hot-fusion reactions (^{20}Ne + ^{235,238}U, ^{16}O + ^{242}Pu, and ^{26}Mg + ^{232}Th), the evaporation residue cross sections calculated by ImQMD model are about an order of magnitude higher than the results calculated by the DNS model.

The reason might be that the DNS model is a semiclassical model, and it does not take the neck development into account, while the microscopic dynamics model ImQMD supposes the formation of a neck between the projectile and target, which is the main characteristic in the collision process. And it is more suitable for hot fusion in which the incident energy is above the Coulomb barrier.

In addition, instead of evolving towards a spherical compound nucleus, the composite systems have a certain probability of splitting up after the projectile nucleus is captured, in the ImQMD model. The number of the events in which the composite system split up is counted and the corresponding split-up probability for fusion reaction is obtained [72]. With the increase of proton number of the system, the

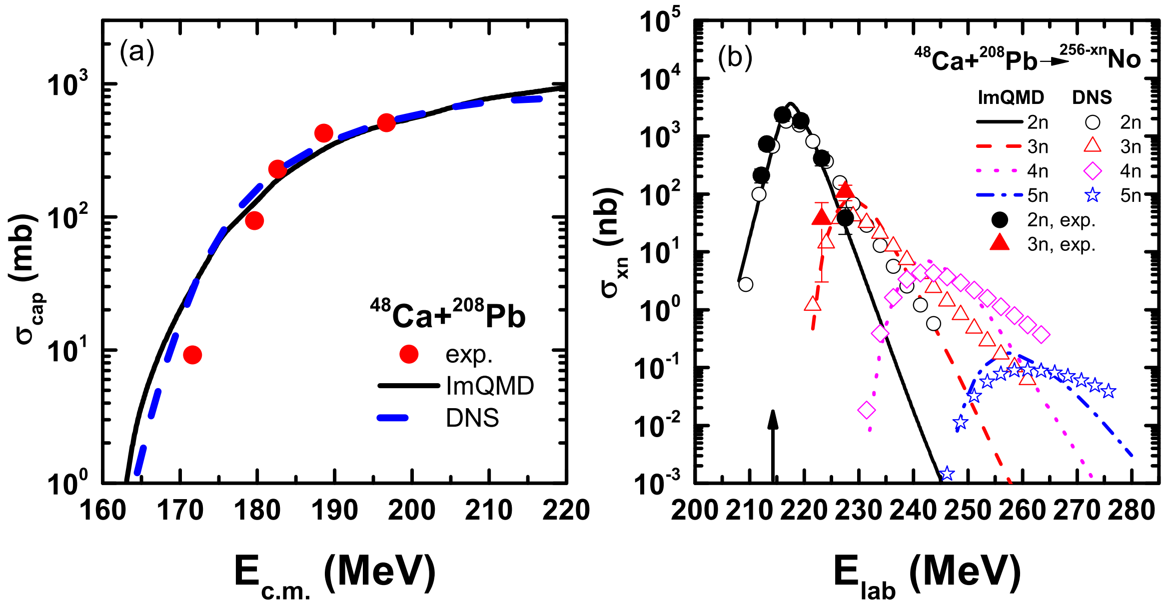

FIG. 2. (a) The capture cross sections of the ^{48}Ca + ^{208}Pb reaction. The solid and dashed lines denote the calculation results from the ImQMD and DNS models, respectively. The experimental data (solid circles) are from Ref. [69]. (b) The excitation functions of the *xn*-evaporation channels ($x = 2$–5) in the reaction ^{48}Ca + ^{208}Pb. The solid, dashed, dotted, and dash-dotted lines indicate calculated results of the 2*n*, 3*n*, 4*n*, and 5*n* channels by the ImQMD model, respectively. The open circles, open triangles, open diamonds, and open five-pointed stars represent calculated results of the 2*n*, 3*n*, 4*n*, and 5*n* channels by the DNS model, respectively. The solid squares and circles represent the available experimental data for the 2*n* and 3*n* channels [70], respectively. The vertical arrow indicates the position of the corresponding Coulomb barrier.

TABLE III. The production cross sections of $^{249-254}$No isotopes in FE reactions. The isotopes, fusion types, and the corresponding reactions are tabulated in columns 1–3. The incident energy $E_{\mathrm{c.m.}}$ and the calculated maximal evaporation residue cross sections for different emission channels via two models (ImQMD and DNS) are listed in columns 4–7. The experimental values of the evaporation residue cross sections σ_{expt} in column 9 are taken from Refs [70,71]. The parts in bold in the table indicate the maximum evaporation residue cross sections of the optimal reactions and energies of these isotopes.

			ImQMD$_{\mathrm{calc}}$		DNS$_{\mathrm{calc}}$			
Isotope	Reaction	Type	$E_{\mathrm{c.m.}}$ (MeV)	$\sigma_{\mathrm{calc}}^{\mathrm{max}}$ (nb)	$E_{\mathrm{c.m.}}$ (MeV)	$\sigma_{\mathrm{calc}}^{\mathrm{max}}$ (nb)	$E_{\mathrm{c.m.}}$ (MeV)	σ_{expt} (nb)
^{249}No	^{208}Pb(^{44}Ca, 3*n*)	Cold	185.0	0.693	182.0	0.709	178.9	0.668
	^{235}U(^{20}Ne, 6*n*)	Hot	132.0	2.535	132.0	0.710		
	^{233}U(^{20}Ne, 4*n*)	**Hot**	**110.0**	**4.702**	**108.0**	**1.986**		
^{250}No	^{208}Pb(^{44}Ca, 2*n*)	Cold	177.0	7.824	176.0	7.243	175.1	1.24 ± 0.5
	^{235}U(^{20}Ne, 5*n*)	Hot	**115.0**	**16.543**	**114.0**	**8.205**		
^{251}No	^{208}Pb(^{48}Ca, 5*n*)	Cold	210.0	0.186	212.0	0.090		
	^{235}U(^{20}Ne, 4*n*)	**Hot**	**107.0**	**19.419**	**102.0**	**10.723**		
^{252}No	^{208}Pb(^{48}Ca, 4*n*)	Cold	197.0	8.020	198.0	4.270		
	^{238}U(^{20}Ne, 6*n*)	Hot	117.0	104.800	118.0	38.756		
	^{242}Pu(^{16}O, 6*n*)	**Hot**	**107.0**	**168.080**	**107.2**	**80.556**		
	^{232}Th(^{26}Mg, 6*n*)	Hot	140.0	16.96632	138.0	12.2462		
^{253}No	^{208}Pb(^{48}Ca, 3*n*)	Cold	186.0	92.355	186.0	41.458	184.9	109 ± 33
	^{238}U(^{20}Ne, 5*n*)	Hot	110.0	137.100	106.0	55.530		
	^{242}Pu(^{16}O, 5*n*)	**Hot**	**92.0**	**465.750**	**93.2**	**81.690**		
	^{232}Th(^{26}Mg, 5*n*)	Hot	127.0	30.44263	128.0	31.410		
^{254}No	**^{208}Pb(^{48}Ca, 2*n*)**	**Cold**	**177.0**	**4289.070**	**176.0**	**1830.01**	175.5	3385 ± 310
	^{238}U(^{20}Ne, 4*n*)	Hot	101.0	287.300	98.0	245.270		
	^{242}Pu(^{16}O, 4*n*)	Hot	85.0	1714.630	85.2	740.330		
	^{232}Th(^{26}Mg, 4*n*)	Hot	115.0	115.9811	122.0	94.130		

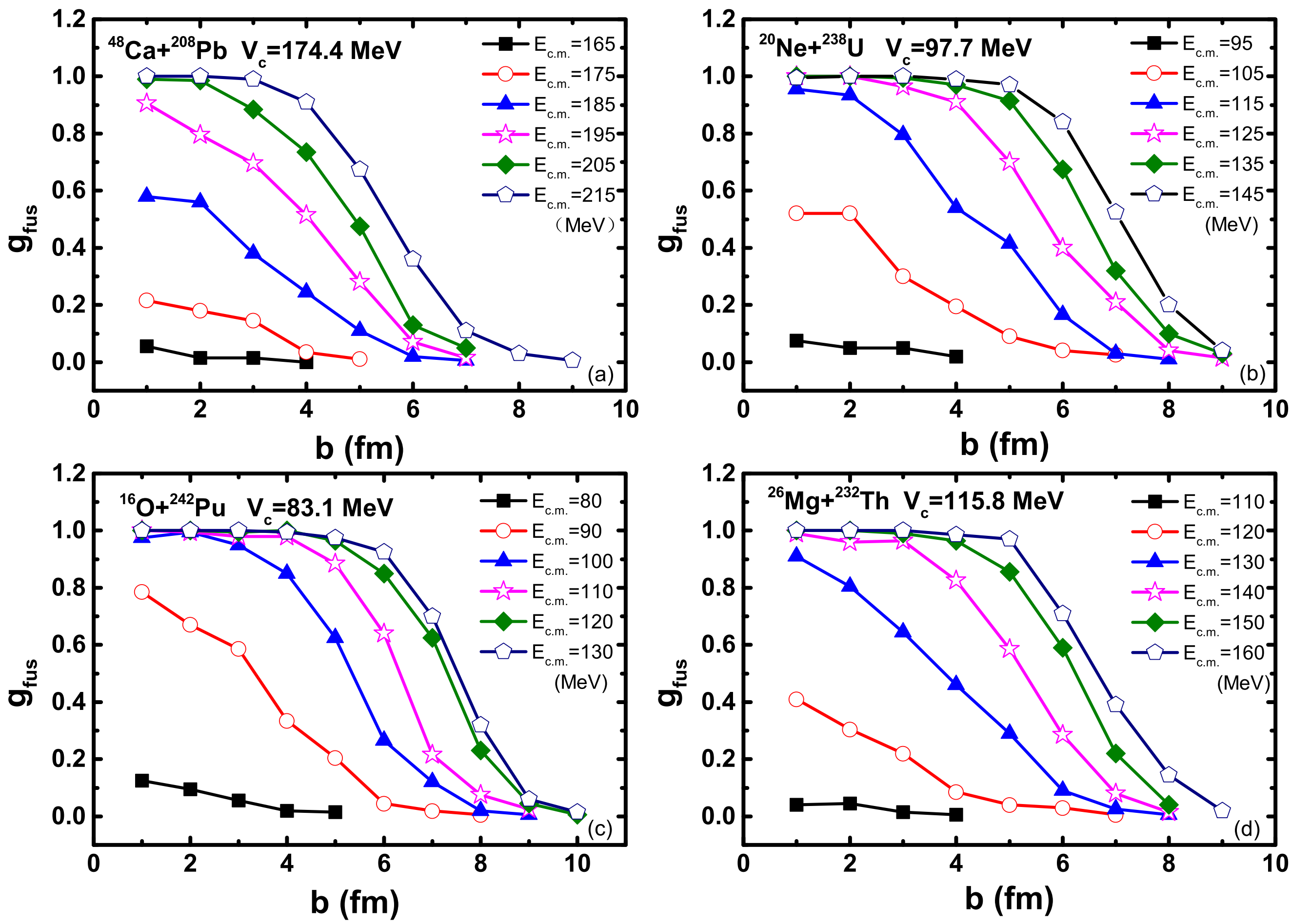

FIG. 3. The fusion probability $g_{\mathrm{fus}}(E_{\mathrm{c.m.}}, b)$ of the different fusion reactions (a) $^{48}\mathrm{Ca} + ^{208}\mathrm{Pb}$, (b) $^{20}\mathrm{Ne} + ^{238}\mathrm{U}$, (c) $^{16}\mathrm{O} + ^{242}\mathrm{Pu}$, and (d) $^{26}\mathrm{Mg} + ^{232}\mathrm{Th}$ at different incident energies with IQ3a parameters as a function of impact parameter b. V_c is the static Coulomb barrier.

split-up probability will increase quickly. The fusion probability is obtained by solving the master equation numerically in DNS model. This possibly causes the evaporation residue cross section calculation to differ from that in the DNS model.

III. RESULTS AND DISCUSSION

A. Fusion probability

Considering that the fusion probability is crucial for predicting the evaporation residue cross sections of the new isotopes with $Z = 102$, the fusion probabilities $g_{\mathrm{fus}}(E_{\mathrm{c.m.}}, b)$ of the four systems are shown in Fig. 3. By comparing Figs. 3(a)–3(d), one can see that the trend of fusion probability with impact parameter b is consistent for the four fusion reaction systems. Here, V_c is the static Coulomb barrier. In the ImQMD simulations, the dynamic barrier is smaller than that obtained with the static Coulomb barrier.

From Fig. 3(a), we can find that at a certain incident energy the fusion probability decreases with the increase of impact parameter. This is because the interaction between two nuclei decreases gradually from central collisions to peripheral collisions, and the probability for fusion reactions decreases and that for elastic scattering processes increases.

In addition, it can also be found that the fusion probability looks like a Fermi distribution at energies above the Coulomb barrier. This means that the fusion probability gradually becomes smaller when the incident energy decreases in Fig. 3. For instance, the fusion probability falls when the incident energy decreases from 215 to 165 MeV for $^{48}\mathrm{Ca} + ^{208}\mathrm{Pb}$. Besides, the fusion events occur at central collisions at energies below V_c, as can also be seen in Figs. 3(a)–3(d).

To understand the formation of a neck between the reaction partners, we study the time evolution of the nuclear density profiles of the projectile and target. Figure 4 shows the time evolution of the density distributions of the projectile and the target in the fusion reaction $^{20}\mathrm{Ne} + ^{238}\mathrm{U}$ at three different incident energies [(a) $E_{\mathrm{c.m.}} = 115$ MeV, (b) $E_{\mathrm{c.m.}} = 125$ MeV, (c) $E_{\mathrm{c.m.}} = 135$ MeV].

From Fig. 4, one can estimate that the formation of the neck stopped at 500, 200, and 200 fm/c for $E_{\mathrm{c.m.}} = 115$ MeV, $E_{\mathrm{c.m.}} = 125$ MeV, $E_{\mathrm{c.m.}} = 135$ MeV, respectively. Comparing the density distributions of the interacting nuclei at the same time ($t = 200$ fm/c) but different incident energies, it can be found that the neck evolution is energy dependent. With the incident energy increases, the nucleon exchange between the reaction partners gets easier, leading to the reduced lifetime of the neck [73].

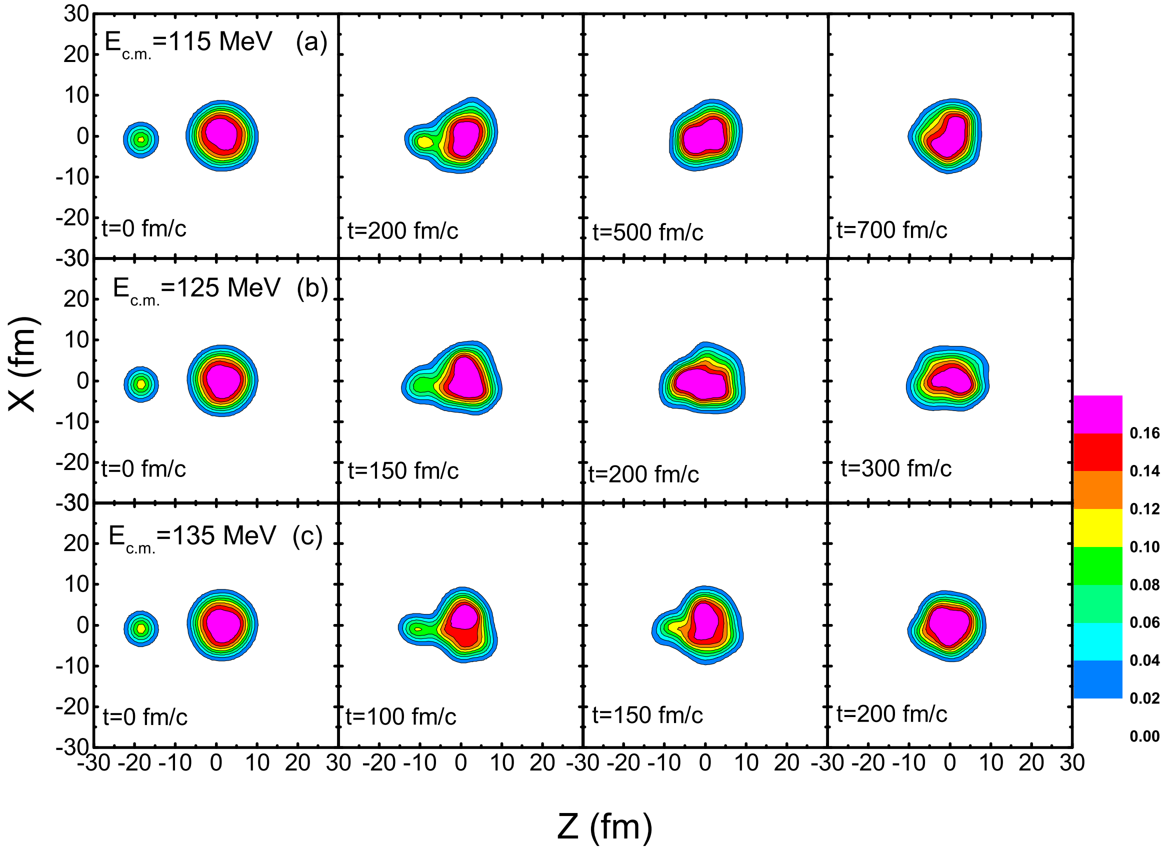

FIG. 4. Time evolution of density profiles for head-on collisions of ^{20}Ne + ^{238}U at three incident energies (a) $E_{\mathrm{c.m.}} = 115$ MeV, (b) $E_{\mathrm{c.m.}} = 125$ MeV, and (c) $E_{\mathrm{c.m.}} = 135$ MeV.

B. The effects of entrance channel on the evaporation residue cross sections

In order to search for the optimal projectile-target combination to produce new neutron-deficient No isotopes, we calculate the evaporation residue cross sections of ^{40,44,48}Ca + ^{208}Pb and ^{20}Ne + ^{233,235,238}U systems correspondingly. For further investigating the effect of different projectile nucleus on the evaporation residue cross sections, we chose ^{40,44,48}Ca as projectiles and the same ^{208}Pb target.

Figure 5 shows the excitation functions for the (a) 2n-evaporation channel, (b) 3n-evaporation channel, (c) 4n-evaporation channel and (d) 5n-evaporation channel of the reactions ^{40,44,48}Ca + ^{208}Pb, respectively. One can find that more neutrons will be emitted with the increase of incident energy in the de-excitation process. Meanwhile, the fission channel becomes more and more important at high excited energies. Hence, the calculated peak values of the 3n, 4n, and 5n channels rapidly decrease compared to that of the 2n channel, especially in the ^{48}Ca + ^{208}Pb reaction.

For the ^{48}Ca + ^{208}Pb reaction, the maximum values of 2n, 3n, 4n and 5n are 4289.070 nb, 92.355 nb, 8.020 nb, and 0.186 nb, respectively, which are the largest among these systems. This is mainly because the addition of 2 neutrons to the projectile increases the chance of survival of the compound nuclei. This is consistent with the results for the ^{62,64}Ni + ^{208}Pb reactions by Hofmann *et al.* [74].

It is also found from Fig. 5(a)–5(d) that the optimum energy of the three reaction systems are quite similar for the same number of evaporating neutrons. Especially in the 5n evaporation channel, the optimal incident energy of three reaction systems are around 210 MeV.

Figure 6 shows the excitation functions in the (a) 4n-evaporation channel, (b) 5n-evaporation channel and (c) 6n-evaporation channel of the reactions ^{20}Ne + ^{233,235,238}U. One can see that the production cross sections in the 4n channel for the ^{20}Ne + ^{238}U reaction are the largest. The optimal energy of the ^{238}U(^{20}Ne, 4n)^{254}No is 101.0 MeV and the corresponding cross sections are around 287.300 nb. Because each neutron emission takes away about 8 MeV energy, it also can be seen that the interval of peaks is about 8 MeV for ^{20}Ne + ^{238}U reaction system among the different evaporation channels.

From Fig. 6, the peak values decrease rapidly with the increasing emitted neutron numbers, which is because the fission becomes more and more important at higher excitation energy. By comparing Fig. 6(a)–6(c), we can see that the peak values of the ^{20}Ne + ^{238}U system are significantly larger than those of ^{20}Ne + ^{233}U and ^{20}Ne + ^{235}U systems in the corresponding neutron evaporation channel. This is because the fusion barrier decreases when the neutron number increases. Neutrons do not contribute to the Coulomb potential energy, but have an enhanced effect on the nuclear potential energy

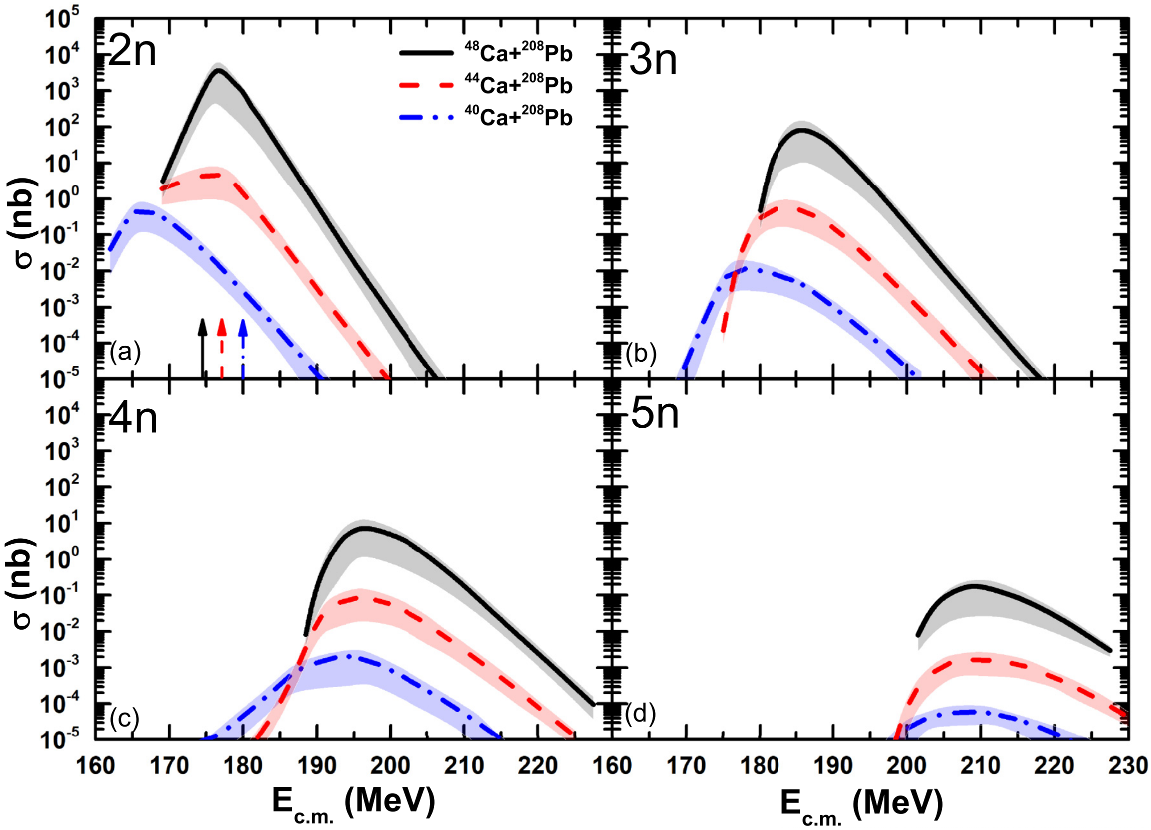

FIG. 5. The calculated excitation functions in the (a) $2n$-evaporation channel, (b) $3n$-evaporation channel, (c) $4n$-evaporation channel, and (d) $5n$-evaporation channel of the reactions $^{40,44,48}Ca + {}^{208}Pb$, respectively. The solid, dashed, and dash-dotted lines indicate the calculated results for the reactions $^{48}Ca + {}^{208}Pb$, $^{44}Ca + {}^{208}Pb$, and $^{40}Ca + {}^{208}Pb$, respectively. The vertical arrows indicate the positions of the corresponding Coulomb barriers. The statistical errors in the calculations are given by the shaded areas.

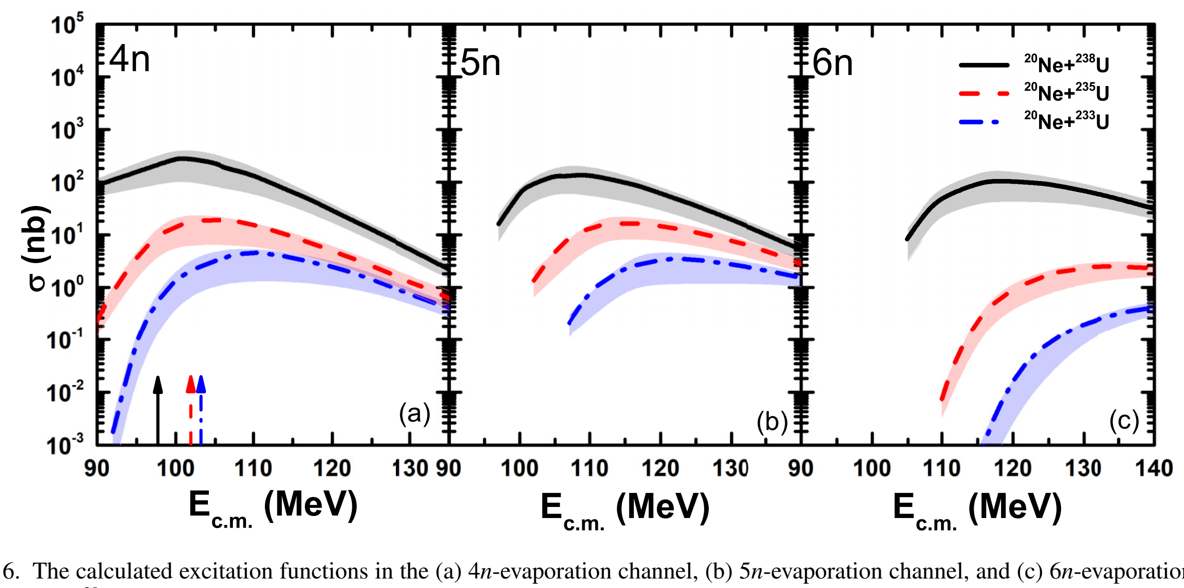

FIG. 6. The calculated excitation functions in the (a) $4n$-evaporation channel, (b) $5n$-evaporation channel, and (c) $6n$-evaporation channel of the reactions $^{20}Ne + {}^{233,235,238}U$, respectively. The solid, dashed, and dash-dotted lines indicate the calculated results for the reactions $^{20}Ne + {}^{238}U$, $^{20}Ne + {}^{235}U$, and $^{20}Ne + {}^{233}U$, respectively. The vertical arrows indicate the positions of the corresponding Coulomb barriers. The statistical errors in the calculations are given by the shaded areas.

in ImQMD model. The another reason is that the compound nucleus ^{253}No is more neutron deficient and has a lower fission barrier compared to ^{258}No and ^{255}No.

Motivated by studying the effects of different projectile-target combinations on the static barrier, we calculated the static barriers in collisions of ^{44}Ca + ^{208}Pb and ^{20}Ne + ^{233}U for the production of nuclei ^{248}No at the optimal incident energy. In Figs. 7(a) and 7(b), one can see that the barriers are 185.33 MeV and 100.80 MeV for the systems ^{44}Ca + ^{208}Pb and ^{20}Ne + ^{233}U, respectively. Besides, the potential pocket depth of ^{20}Ne + ^{233}U fusion reaction system is larger than that in ^{44}Ca + ^{208}Pb reaction system.

It is found that the ^{20}Ne + ^{233}U is a promising candidate to produce ^{248}No. This is mainly because the height of the static barrier gradually decrease with the increase of the mass asymmetry of projectile and target. The deeper potential valley of the barrier indicates the higher mass asymmetry of the projectile-target, and the easier for the nucleus to be captured [75].

C. Production cross sections of unknown neutron-deficient $^{243-248}$No isotopes

The evaporation residue cross sections of unknown $^{243-248}$No isotopes via different reactions at corresponding incident energies with ImQMD model and DNS model are given in Table IV. From Table IV, the neutron-deficient $^{243-246}$No can be synthesized within the cold-fusion mechanism, while the rest of unknown isotopes ^{247,248}No are synthesized within the hot-fusion mechanism by ^{233}U(^{20}Ne, 6n) ^{247}No and ^{233}U(^{20}Ne, 5n) ^{248}No.

It is obvious that yield becomes lower with more neutrons evaporating in the same projectile-target combination due to the fission channels becomes more important in the high energy deexcitation process. The largest corresponding evaporation residue cross sections (the incident energy) of the $^{243-248}$No calculated by the ImQMD model are 0.061 pb ($E_{\text{c.m.}}$ = 210.0 MeV), 2.250 pb ($E_{\text{c.m.}}$ = 193.0 MeV), 0.005 nb ($E_{\text{c.m.}}$ = 185.0 MeV), 0.530 nb ($E_{\text{c.m.}}$ = 165.0 MeV), 0.432 nb ($E_{\text{c.m.}}$ = 145.0 MeV), and 3.518 nb ($E_{\text{c.m.}}$ = 122.0 MeV), respectively.

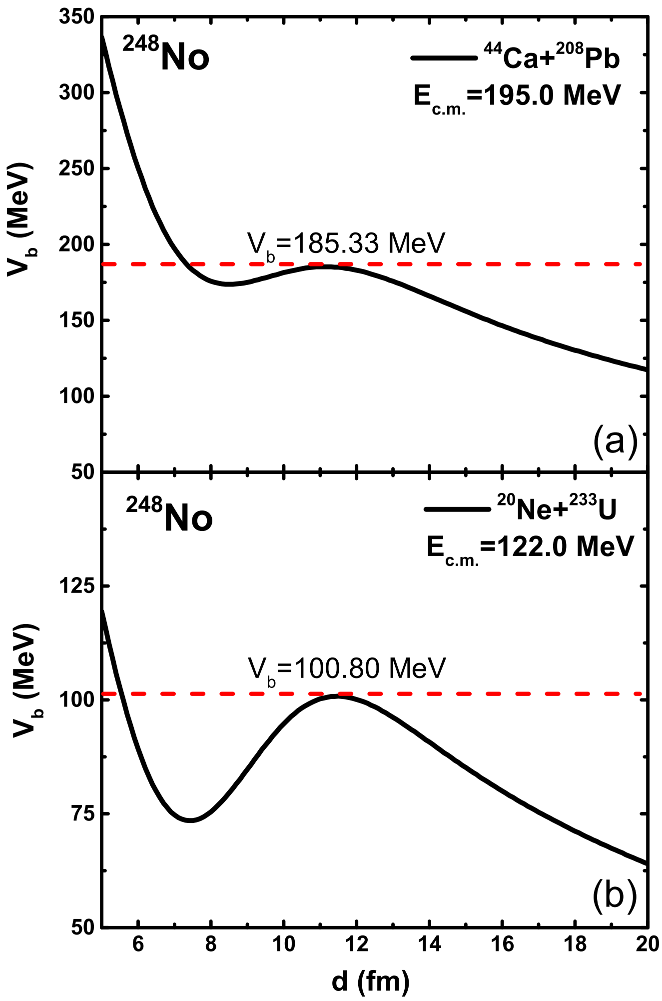

FIG. 7. The static barriers in collisions of ^{44}Ca + ^{208}Pb and ^{20}Ne + ^{233}U for the production of nuclei ^{248}No at the optimal incident energy.

In Fig. 8, the heavy nuclei region near No ($Z = 102$) on the nuclear map is shown. The filled and open squares denote the known and unknown nuclei, respectively. Olive, yellow, and red colors show the spontaneous fission, α decay, and β^+

TABLE IV. The production cross sections of $^{243-248}$No isotopes in FE reactions. The isotopes, fusion types, and the corresponding reactions are tabulated in columns 1–3. The incident energy $E_{\text{c.m.}}$ and the calculated maximal evaporation residue cross sections for different emission channels via two models (ImQMD and DNS) are listed in columns 4–7. The parts in bold in the table indicate the maximum evaporation residue cross sections of the optimal reactions and energies of these isotopes.

			ImQMD$_{\text{calc}}$		DNS$_{\text{calc}}$	
Isotope	Reaction	Type	$E_{\text{c.m.}}$ (MeV)	$\sigma^{\max}_{\text{calc}}$ (nb)	$E_{\text{c.m.}}$ (MeV)	$\sigma^{\max}_{\text{calc}}$ (nb)
^{243}No	^{208}Pb(^{40}Ca, 5n)	Cold	210.0	6.080×10^{-05}	207.0	1.495×10^{-04}
^{244}No	^{208}Pb(^{40}Ca, 4n)	Cold	193.0	2.250×10^{-03}	197.0	6.510×10^{-03}
^{245}No	^{208}Pb(^{40}Ca, 3n)	Cold	185.0	0.005	179.0	0.010
^{246}No	^{208}Pb(^{40}Ca, 2n)	Cold	165.0	0.530	167.0	0.414
^{247}No	^{208}Pb(^{44}Ca, 5n)	Cold	210.0	0.002	216.0	0.002
	^{233}U(^{20}Ne, 6n)	**Hot**	**145.0**	**0.432**	**126.0**	**0.016**
^{248}No	^{208}Pb(^{44}Ca, 4n)	Cold	195.0	0.089	198.0	0.076
	^{233}U(^{20}Ne, 5n)	**Hot**	**122.0**	**3.518**	**122.0**	**1.193**

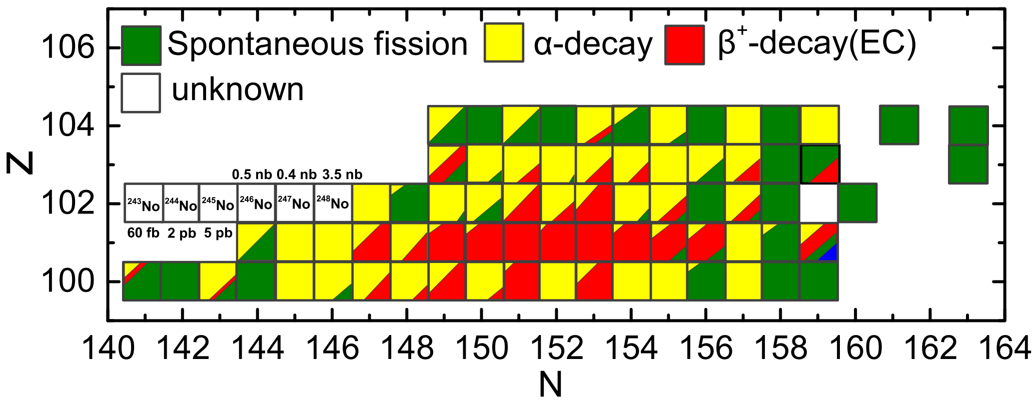

FIG. 8. Heavy nuclei region near No ($Z = 102$) on the nuclear map. The filled and open squares denote the known and unknown nuclei, respectively. Olive, yellow, and red colors show the spontaneous fission, α decay, and β^+ decay, respectively. The production cross sections of unknown No isotopes are indicated in the figure.

decay, respectively. The production cross sections of unknown No isotopes are indicated in the figure. One can find clearly from the nuclear map that six unknown neutron-deficient $^{243-248}$No isotopes, with maximum evaporation residue cross sections 0.061 pb, 2.250 pb, 0.005 nb, 0.530 nb, 0.432 nb, and 3.518 nb, can be produced respectively.

IV. CONCLUSIONS

The synthesis of No isotopes ($^{243-248}$No) is studied in fusion reactions based on the ImQMD model with a statistical model. This work compares the calculation results of capture cross sections and evaporation residue cross sections with the experimental data of the reaction ^{48}Ca + ^{208}Pb. The calculated results are in good agreement with the experimental data. The effects of the impact parameter and incident energy on fusion probability are studied. At a certain incident energy, the fusion probability decreases with the increase of impact parameter. Besides, the fusion probability falls when the incident energy decreases for the same fusion reactions. The lifetime of the neck plays an important role in fusion process, and the time of neck formation is energy dependent. By comparing the production cross sections of the reactions ^{40,44,48}Ca + ^{208}Pb and ^{20}Ne + ^{233,235,238}U, it is found that an increase of the neutron number of the projectile or target would lead to an increase of the evaporation residue cross sections. The effects of different projectile-target combinations have also been studied in the reactions ^{44}Ca + ^{208}Pb and ^{20}Ne + ^{233}U, and we find that ^{20}Ne + ^{233}U is a good combination to produce the ^{248}No isotope. Six unknown neutron-deficient isotopes $^{243-248}$No are predicted with maximum evaporation residue cross sections 0.061 pb, 2.250 pb, 0.005 nb, 0.530 nb, 0.432 nb, and 3.518 nb, respectively.

ACKNOWLEDGMENTS

This work was supported by the National Natural Science Foundation of China under Grants No. 12135004, No. 11635003, No. 11961141004, No. 12105019, and No. 12047513, and by the Beijing Postdoctoral Research Foundation (2021-zz-089).

[1] A. Sobiczewski, F. A. Gareev, and B. N. Kalinkin, Phys. Lett **22**, 500 (1966).
[2] G. Mönzenberg, S. Hofmann, F. P. Heßberger, W. Reisdorf, K. H. Schmidt, J. H. R. Schneider, P. Armbruster, C. C. Sahm, and B. Thuma, Z. Phys. A **300**, 107 (1981).
[3] G. Münzenberg, P. Armbruster, H. Folger, F. P. Heßberger, S. Hofmann, J. Keller, K. Poppensieker, W. Reisdorf, K. H. Schmidt, H. J. Schött, M. E. Leino, and R. Hingmann, Z. Phys. A **317**, 235 (1984).
[4] G. Mönzenberg, P. Armbruster, F. P. Heßberger, S. Hofmann, K. Poppensieker, W. Reisdorf, J. H. R. Schneider, W. F. W. Schneider, K. H. Schmidt, C. C. Sahm, and D. Vermeulen, Z. Phys. A **309**, 89 (1982).
[5] S. Hofmann, V. Ninov, F. P. Heßberger, P. Armbruster, H. Folger, G. Münzenberg, H. J. Schött, A. G. Popeko, A. V. Yeremin, A. N. Andreyev, S. Saro, R. Janik, and M. Leino, Z. Phys. A **350**, 277 (1995).
[6] S. Hofmann, V. Ninov, F. P. Heßberger, P. Armbruster, H. Folger, G. Münzenberg, H. J. Schött, A. G. Popeko, A. V. Yeremin, A. N. Andreyev, S. Saro, R. Janik, and M. Leino, Z. Phys. A **350**, 281 (1995).
[7] S. Hofmann, V. Ninov, F. P. Heßberger, P. Armbruster, H. Folger, G. Münzenberg, H. J. Schött, A. G. Popeko, A. V. Yeremin, S. Saro, R. Janik, and M. Leino, Z. Phys. A **354**, 229 (1996).
[8] Y. T. Oganessian, V. K. Utyonkov, Y. V. Lobanov, F. S. Abdullin, A. N. Polyakov, I. V. Shirokovsky, Y. S. Tsyganov, G. G. Gulbekian, S. L. Bogomolov, B. N. Gikal, A. N. Mezentsev, S. Iliev, V. G. Subbotin, A. M. Sukhov, A. A. Voinov, G. V. Buklanov, K. Subotic, V. I. Zagrebaev, M. G. Itkis, J. B. Patin *et al.*, Phys. Rev. C **69**, 054607 (2004).
[9] K. Morita, K. Morimoto, D. Kaji, T. Akiyama, S. Goto, H. Haba, E. Ideguchi, R. Kanungo, K. Katori, H. Koura, H. Kudo, T. Ohnishi, A. Ozawa, T. Suda, K. Sueki, H. S. Xu, T.

Yamaguchi, A. Yoneda, A. Yoshida, and Y. L. Zhao, J. Phys. Soc. Jpn. **73**, 2593 (2004).

[10] Y. T. Oganessian, V. K. Utyonkov, Y. V. Lobanov, F. S. Abdullin, A. N. Polyakov, R. N. Sagaidak, I. V. Shirokovsky, Y. S. Tsyganov, A. A. Voinov, G. G. Gulbekian, S. L. Bogomolov, B. N. Gikal, A. N. Mezentsev, V. G. Subbotin, A. M. Sukhov, K. Subotic, V. I. Zagrebaev, G. K. Vostokin, M. G. Itkis *et al.*, Phys. Rev. C **76**, 011601 (2007).

[11] Y. T. Oganessian, V. K. Utyonkoy, Y. V. Lobanov, F. S. Abdullin, A. N. Polyakov, I. V. Shirokovsky, Y. S. Tsyganov, G. G. Gulbekian, S. L. Bogomolov, A. N. Mezentsev, S. Iliev, V. G. Subbotin, A. M. Sukhov, A. A. Voinov, G. V. Buklanov, K. Subotic, V. I. Zagrebaev, M. G. Itkis, J. B. Patin, K. J. Moody *et al.*, Phys. Rev. C **69**, 021601(R) (2004).

[12] Y. T. Oganessian, V. K. Utyonkov, Y. V. Lobanov, F. S. Abdullin, A. N. Polyakov, I. V. Shirokovsky, Y. S. Tsyganov, G. G. Gulbekian, S. L. Bogomolov, B. N. Gikal, A. N. Mezentsev, S. Iliev, V. G. Subbotin, A. M. Sukhov, A. A. Voinov, G. V. Buklanov, K. Subotic, V. I. Zagrebaev, M. G. Itkis, J. B. Patin *et al.*, Phys. Rev. C **70**, 064609 (2004).

[13] Y. T. Oganessian, F. S. Abdullin, P. D. Bailey, D. E. Benker, M. E. Bennett, S. N. Dmitriev, J. G. Ezold, J. H. Hamilton, R. A. Henderson, M. G. Itkis, Y. V. Lobanov, A. N. Mezentsev, K. J. Moody, S. L. Nelson, A. N. Polyakov, C. E. Porter, A. V. Ramayya, F. D. Riley, J. B. Roberto, M. A. Ryabinin *et al.*, Phys. Rev. Lett. **104**, 142502 (2010).

[14] P. A. Ellison, K. E. Gregorich, J. S. Berryman, D. L. Bleuel, R. M. Clark, I. Dragojević, J. Dvorak, P. Fallon, C. Fineman-Sotomayor, J. M. Gates, O. R. Gothe, I. Y. Lee, W. D. Loveland, J. P. McLaughlin, S. Paschalis, M. Petri, J. Qian, L. Stavsetra, M. Wiedeking, and H. Nitsche, Phys. Rev. Lett. **105**, 182701 (2010).

[15] Y. T. Oganessian, V. K. Utyonkov, Y. V. Lobanov, F. S. Abdullin, A. N. Polyakov, R. N. Sagaidak, I. V. Shirokovsky, Y. S. Tsyganov, A. A. Voinov, G. G. Gulbekian, S. L. Bogomolov, B. N. Gikal, A. N. Mezentsev, S. Iliev, V. G. Subbotin, A. M. Sukhov, K. Subotic, V. I. Zagrebaev, G. K. Vostokin, M. G. Itkis *et al.*, Phys. Rev. C **74**, 044602 (2006).

[16] T. Sumita, K. Morimoto, D. Kaji, H. Haba, K. Ozeki, R. Sakai, A. Yoneda, A. Yoshida, H. Hasebe, K. Katori, N. Sato, Y. Wakabayashi, S. Mitsuoka, S. Goto, M. Murakami, Y. Kariya, F. Tokanai, K. Mayama, M. Takeyama, T. Moriya *et al.*, J. Phys. Soc. Jpn. **82**, 024202 (2013).

[17] V. K. Utyonkov, N. T. Brewer, Y. T. Oganessian, K. P. Rykaczewski, F. S. Abdullin, S. N. Dmitriev, R. K. Grzywacz, M. G. Itkis, K. Miernik, A. N. Polyakov, J. B. Roberto, R. N. Sagaidak, I. V. Shirokovsky, M. V. Shumeiko, Y. S. Tsyganov, A. A. Voinov, V. G. Subbotin, A. M. Sukhov, A. V. Sabel'nikov, G. K. Vostokin *et al.*, Phys. Rev. C **92**, 034609 (2015).

[18] E. D. Donets, V. A. Shchegolev, and V. A. Ermakov, At. Energ **20**, 257 (1966).

[19] B. A. Zager, M. B. Miller, V. L. Mikheev, S. M. Polikanov, A. M. Sukhov, G. N. Flerov, and L. P. Chelnokov, Sov. At. Energy **20**, 264 (1966).

[20] A. I. Svirikhin, A. V. Yeremin, N. I. Zamyatin, I. N. Izosimov, A. V. Isaev, A. A. Kuznetsova, O. N. Malyshev, R. S. Mukhin, A. G. Popeko, Y. A. Popov, E. A. Sokol, B. Sailaubekov, M. S. Tezekbayeva, M. L. Chelnokov, V. I. Chepigin, B. Andel, S. Antalic, A. Bronis, P. Mosat, B. Gall *et al.*, Phys. Part. Nucl. Lett **18**, 445 (2021).

[21] J. Khuyagbaatar, H. Brand, R. A. Cantemir, C. E. Düllmann, F. P. Heßberger, E. Jäger, B. Kindler, J. Krier, N. Kurz, B. Lommel, B. Schausten, and A. Yakushev, Phys. Rev. C **104**, L031303 (2021).

[22] Y. T. Oganessian, V. K. Utyonkov, Y. V. Lobanov, F. S. Abdullin, A. N. Polyakov, I. V. Shirokovsky, Y. S. Tsyganov, A. N. Mezentsev, S. Iliev, V. G. Subbotin, A. M. Sukhov, K. Subotic, O. V. Ivanov, A. N. Voinov, V. I. Zagrebaev, K. J. Moody, J. F. Wild, N. J. Stoyer, M. A. Stoyer, and R. W. Lougheed, Phys. Rev. C **64**, 054606 (2001).

[23] A. Ghiorso, T. Sikkeland, and M. J. Nurmia, Phys. Rev. Lett. **18**, 401 (1967).

[24] V. L. Mikheev, V. I. Ilyushchenko, M. B. Miller, S. M. Polikanov, G. N. Flerov, and Y. P. Kharitonov, Sov. At. Energy **22**, 93 (1967).

[25] V. A. Druin, G. N. Akap'ev, A. G. Demin, Y. V. Lobanov, B. V. Fefilov, G. N. Flerov, and L. P. Chelnokov, At. Energ. **22**, 135 (1967).

[26] E. Donets, V. Shchegolets, and V. Ermakov, At. Energ. **16**, 233 (1964).

[27] E. K. Hulet, J. F. Wild, R. J. Dougan, R. W. Lougheed, J. H. Landrum, A. D. Dougan, P. A. Baisden, C. M. Henderson, R. J. Dupzyk, R. L. Hahn, M. Schädel, K. Sümmerer, and G. R. Bethune, Phys. Rev. C **40**, 770 (1989).

[28] R. J. Silva, P. F. Dittner, M. L. Mallory, O. L. Keller, K. Eskola, P. Eskola, M. Nurmia, and A. Ghiorso, Nucl. Phys. A **216**, 97 (1973).

[29] L. P. Somerville, M. J. Nurmia, J. M. Nitschke, A. Ghiorso, E. K. Hulet, and R. W. Lougheed, Phys. Rev. C **31**, 1801 (1985).

[30] G. T. Seaborg, J. Nucl. Mater. **166**, 22 (1989).

[31] A. N. Andreyev, D. D. Bogdanov, V. I. Chepigin, A. P. Kabachenko, O. N. Malyshev, R. N. Sagaidak, L. I. Salamatin, G. M. Ter-Akopian, and A. V. Yeremin, Z. Phys. A **345**, 389 (1993).

[32] A. V. Yeremin, O. N. Malyshev, A. G. Popeko, V. I. Chepigin, A. I. Svirikhin, A. Lopez-Martens, K. Hauschild, O. Dorvaux, B. Gall, and J. Gehlot, EPJ Web. Conf. **345**, 00065 (2015).

[33] K. Kessaci, B. J. P. Gall, O. Dorvaux, A. Lopez-Martens, R. Chakma, K. Hauschild, M. L. Chelnokov, V. I. Chepigin, M. Forge, A. V. Isaev, I. N. Izosimov, D. E. Katrasev, A. A. Kuznetsova, O. N. Malyshev, R. Mukhin, J. Piot, A. G. Popeko, Y. A. Popov, E. A. Sokol, A. I. Svirikhin *et al.*, Phys. Rev. C **104**, 044609 (2021).

[34] L. Liu, C. Shen, Q. Li, Y. Tu, X. Wang, and Y. Wang, Eur. Phys. J. A **52**, 35 (2016).

[35] G. Adamian, N. Antonenko, and W. Scheid, Nucl. Phys. A **618**, 176 (1997).

[36] G. Adamian, N. Antonenko, W. Scheid, and V. Volkov, Nucl. Phys. A **627**, 361 (1997).

[37] Z. Q. Feng, G. M. Jin, and J. Q. Li, Phys. Rev. C **80**, 057601 (2009).

[38] L. Zhu, J. Su, and F. S. Zhang, Phys. Rev. C **93**, 064610 (2016).

[39] X. J. Bao, S. Q. Guo, H. F. Zhang, and J. Q. Li, Phys. Rev. C **96**, 024610 (2017).

[40] Z. H. Liu and J. D. Bao, Phys. Rev. C **80**, 054608 (2009).

[41] Z. H. Liu and J. D. Bao, Phys. Rev. C **81**, 044606 (2010).

[42] K. Siwek-Wilczyńska, T. Cap, M. Kowal, A. Sobiczewski, and J. Wilczyński, Phys. Rev. C **86**, 014611 (2012).

[43] N. Ghahramany and A. Ansari, Eur. Phys. J. A **52**, 287 (2016).

[44] K. P. Santhosh and V. Safoora, Eur. Phys. J. A **54**, 80 (2018).

[45] V. I. Zagrebaev, A. V. Karpov, and W. Greiner, Phys. Rev. C **85**, 014608 (2012).
[46] N. Rowley and K. Hagino, Phys. Rev. C **91**, 044617 (2015).
[47] J. J. Li, C. Li, G. Zhang, L. Zhu, Z. Liu, and F. S. Zhang, Phys. Rev. C **95**, 054612 (2017).
[48] S. Ayik, B. Yilmaz, O. Yilmaz, and A. S. Umar, Phys. Rev. C **97**, 054618 (2018).
[49] S. Ayik, B. Yilmaz, O. Yilmaz, and A. S. Umar, Phys. Rev. C **100**, 014609 (2019).
[50] Z. J. Wu and L. Guo, Phys. Rev. C **100**, 014612 (2019).
[51] Z. J. Wu, L. Guo, Z. Liu, and G. X. Peng, Phys. Lett. B **825**, 136886 (2022).
[52] C. Li, X. X. Xu, J. J. Li, G. Zhang, B. Li, C. A. T. Sokhna, Z. S. Ge, F. Zhang, P. W. Wen, and F. S. Zhang, Phys. Rev. C **99**, 024602 (2019).
[53] K. Zhao, Z. Liu, F. S. Zhang, and N. Wang, Phys. Lett. B **815**, 136101 (2021).
[54] H. Wolter, M. Colonna, D. Cozma, P. Danielewicz, C. M. Ko, R. Kumar, A. Ono, M. B. Tsang, J. Xu, Y. X. Zhang, E. Bratkovskaya, Z. Q. Feng, T. Gaitanos, A. L. Fevre, N. Ikeno, Y. Kim, S. Mallik, P. Napolitani, D. Oliinychenko, T. Ogawa, Prog. Part. Nucl. Phys **125**, 103962 (2022).
[55] J. Aichelin, Phys. Rep **202**, 233 (1991).
[56] N. Wang, Z. X. Li, and X. Z. Wu, Phys. Rev. C **65**, 064608 (2002).
[57] M. Papa, T. Maruyama, and A. Bonasera, Phys. Rev. C **64**, 024612 (2001).
[58] J. Xu and C. M. Ko, Phys. Rev. C **94**, 054909 (2016).
[59] N. Wang, L. Ou, Y. X. Zhang, and Z. X. Li, Phys. Rev. C **89**, 064601 (2014).
[60] W. Reisdorf, Z. Phys. A **300**, 227 (1981).
[61] W. Reisdorf and M. Schädel, Z. Phys. A **343**, 47 (1992).
[62] R. J. Charity, M. A. McMahan, G. J. Wozniak, R. J. McDonald, L. G. Moretto, D. G. Sarantites, L. G. Sobotka, G. Guarino, A. Pantaleo, L. Fiore, A. Gobbi, and K. D. Hildenbrand, Nucl. Phys. A **483**, 371 (1988).
[63] G. G. Adamian, N. V. Antonenko, W. Scheid, and V. V. Volkov, Nucl. Phys. A **633**, 409 (1998).
[64] P. Moller, J. R. Nix, W. D. Myers, and W. J. Swiatecki, At. Data Nucl. Data Tables **59**, 185 (1995).
[65] E. A. Cherepanov, A. S. Iljinov, and M. V. Mebel, J. Phys. G **9**, 931 (1983).
[66] Z. Q. Feng, G. M. Jin, J. Q. Li, and W. Scheid, Phys. Rev. C **76**, 044606 (2007).
[67] A. S. Zubov, G. G. Adamian, N. V. Antonenko, S. P. Ivanova, and W. Scheid, Phys. Rev. C **65**, 024308 (2002).
[68] J. D. Jackson, Can. J. Phys **34**, 767 (1956).
[69] E. V. Prokhorova, A. A. Bogchev, M. G. Itkis, I. M. Itkis, G. N. Knyazheva, N. A. Kondratiev, E. M. Kozulin, L. Krupa, Y. T. Oganessian, I.V. Pokrovsky, V. V. Pashkevich, and A. Y. Rusanov, Nucl. Phys. A **802**, 45 (2008).
[70] H. W. Gäggeler, D. T. Jost, A. Türler, P. Armbruster, W. Brüchle, H. Folger, F. P. Heßberger, S. Hofmann, G. Müzenberg, V. Ninov, W. Reisdorf, M. Schädel, K. Sümmerer, J. V. Kratz, U. Scherer, and M. E. Leino, Nucl. Phys. A **502**, 561 (1989).
[71] A. V. Belozerov, M. L. Chelnokov, V. I. Chepigin, T. P. Drobina, V. A. Gorshkov, A. P. Kabachenko, O. N. Malyshev, I. M. Merkin, Y. T. Oganessian, A. G. Popeko, R. N. Sagaidak, A. I. Svirikhin, A. V. Yeremin, G. Berek, I. Brida, and Š. Šáro, Eur. Phys. J. A **16**, 447 (2003).
[72] N. Wang, Z. X. Li, X. Z. Wu, and E. G. Zhao, Mod. Phys. Lett. A **20**, 2619 (2005).
[73] V. Zanganeh, R. Gharaei, and N. Wang, Phys. Rev. C **95**, 034620 (2017).
[74] S. Hofmann, Rep. Prog. Phys. **61**, 639 (1998).
[75] V. Y. Denisov and W. Nörenberg, Eur. Phys. J. A **15**, 375 (2002).